

THE OFFICIAL MAGAZINE OF THE OCEANOGRAPHY SOCIETY

Oceanography

CITATION

Gordon, A.L., C.F. Giulivi, J. Busecke, and F.M. Bingham. 2015. Differences among subtropical surface salinity patterns. *Oceanography* 28(1):32–39, <http://dx.doi.org/10.5670/oceanog.2015.02>.

DOI

<http://dx.doi.org/10.5670/oceanog.2015.02>

COPYRIGHT

This article has been published in *Oceanography*, Volume 28, Number 1, a quarterly journal of The Oceanography Society. Copyright 2015 by The Oceanography Society. All rights reserved.

USAGE

Permission is granted to copy this article for use in teaching and research. Republication, systematic reproduction, or collective redistribution of any portion of this article by photocopy machine, reposting, or other means is permitted only with the approval of The Oceanography Society. Send all correspondence to: info@tos.org or The Oceanography Society, PO Box 1931, Rockville, MD 20849-1931, USA.

Differences Among Subtropical Surface Salinity Patterns

By Arnold L. Gordon, Claudia F. Giulivi,
Julius Busecke, and Frederick M. Bingham

ABSTRACT. The subtropical ocean, exposed to evaporation excess over precipitation, is characterized by regional sea surface salinity maxima (SSS-max). Ocean circulation and mixing processes inject freshwater, establishing a quasi-steady state, though imbalances across the time spectrum result in periods of increasing and decreasing SSS-max. The integrated effect of the array of atmospheric and oceanic forces governing sea surface salinity is shaped by the specific regional ocean basin configuration as well as their coupling to the global ocean system, resulting in SSS-max patterns and locations that display marked differences between the subtropical regimes. We provide a brief description of the SSS-max characteristics of the five subtropical regimes and present aspects of their regional settings that may account for their dissimilarities.

INTRODUCTION

Dry conditions define the subtropical climate belt around our planet, a consequence of the descending limb of the atmospheric subtropical Hadley cell, which is marked by deserts on land and salty surface ocean water. However, the characteristics of the subtropical climate belt vary as land/ocean configurations impose regional differences. The subtropical atmosphere imprints a distinct salinity pattern onto the surface ocean, which is further shaped by ocean circulation and mixing. As part of the shallow

overturning circulation, this composes a vital component of the marine hydrological cycle (McCreary and Lu, 1994; Schmitt, 1995; 2008; Talley, 2002, 2008; Schanze et al., 2010).

Subtropical sea surface salinity maxima (SSS-max) have been well-known features since the early days of descriptive oceanography. As in situ data sets grow, most notably with the advent of the Argo float array (<http://www.argo.ucsd.edu>), we are gaining an ever more detailed view of sea surface salinity, allowing us to go beyond the climatic mean to delve

into temporal fluctuations. Recent additions to our observational toolkit are near synoptic, near global views of SSS from orbiting satellites: the National Aeronautics and Space Administration/Comisión Nacional de Actividades Espaciales (NASA/CONAE) Aquarius/SAC-D and the European Space Agency's Soil Moisture and Ocean Salinity (SMOS) missions, which have greatly extended our ability to chart SSS spatial patterns and temporal behavior. Adding SSS to the arsenal of satellite data is revolutionizing oceanography, enabling more quantitative investigation of ocean dynamics, the processes governing the SSS field, and the associated marine hydrological cycle. The field program Salinity Processes in the Upper-ocean Regional Study (SPURS), using a broad array of in situ observations in the subtropical North Atlantic SSS-max, combined with the satellite data stream, provides new insights into the salinity observations and the physical processes that affect salinity.

To place the SPURS North Atlantic SSS-max view into perspective, we compare the SSS-max patterns for five subtropical regimes and discuss the underlying causes of these differences (for further description of the SSS-max, see the World Ocean Circulation Experiment atlas series for the Atlantic, Pacific, and Indian Oceans: Koltermann et al., 2011; Talley, 2007, 2011, respectively; as well as standard textbooks, e.g., Talley et al., 2011). We use climatological data, monthly Aquarius SSS data for 2012–2013, and Argo data for 2011–2013. The SSS-max patterns are placed within the fields of evaporation–precipitation, Ekman transport, and dynamic topography. The five subtropical regimes are those of the North and South Atlantic, the North and South Pacific, and the southern Indian Oceans. Not included is the unique situation of the monsoon-dominated Indian Ocean north of the equator, which is composed of two large embayments: the salty Arabian Sea and the fresher Bay of Bengal.

DATA

To describe the subtropical SSS-max climatology, we use the Monthly Isopycnal/Mixed Layer Ocean Climatology (MIMOC; <http://www.pmel.noaa.gov/mimoc>; Schmidtko et al., 2013). This optimal interpolated data set is provided as gridded data with a spatial resolution of $0.5^\circ \times 0.5^\circ$ on selected standard pressure levels from the surface to the 1,950 dbar level. The climatology is a long-term average, with values provided for each month, and it is based mostly on Argo data, supplemented by shipboard and conductivity-temperature-depth (CTD) data.

For recent years, in particular the 2011–2013 period, we analyze SSS from an in situ observational based gridded product and from remote satellite measurements. The in situ derived gridded product, generated by the Japan Agency for Marine-Earth Science and Technology (JAMSTEC) as part of the Japan Argo Delayed-Mode Data Base, is the MOAA

GPV (Grid Point Value of the Monthly Objective Analysis using the Argo data). This data set is a monthly global analysis of temperature and salinity mapped by optimal interpolation based on Argo, TRITON (Triangle Trans-Ocean Buoy Network), and available CTD data since January 2001 (Hosoda et al., 2008) on a 1° grid in the global ocean and from 10 to 2,000 dbar (http://www.jamstec.go.jp/ARGO/J_ARGOe.html). For the satellite-derived SSS, we use data from the Aquarius/SAC-D satellite mission (Lagerloef et al., 2008, 2012; Lagerloef, 2012), providing, since August 2011, global SSS maps every seven days. The latest available version of Aquarius salinity (V3.0) has been greatly improved, with an overall accuracy for monthly 150 km averages estimated to be 0.265. This number is based on an intercomparison of SSS measurements from Aquarius and Argo floats and model salinity field from HYCOM (<http://www.hycom.org>). Over most of the open ocean, the errors are less than 0.2 psu (Lagerloef et al., 2013; Meissner et al., 2014). Aquarius retrieves the salinity over the top few centimeters of the ocean using a microwave radiometer and a scatterometer to account for surface roughness. In our study, we use the monthly 1° latitude/longitude gridded (Level-3) version 3.0 SSS bias adjusted product downloaded from NASA PO.DAAC (<ftp://podaac-ftp.jpl.nasa.gov/allData/aquarius/L3>). The SSS-max regions are located over the open ocean in relatively calm and warm subtropical regions, far from continents (except for the South Atlantic SSS-max), which minimizes radio frequency interference, surface roughness, and cold sea surface temperature (SST) problems. To avoid any further contamination of the Aquarius SSS signal close to the coast or islands, any data closer than 3° to land are masked out.

Although we expect good agreement between the in situ and satellite gridded SSS measurements, we note that these data sets are independent, with their own limitations and spatial and temporal resolutions, and gridded with different

methods. Aquarius measures the skin layer salinity of the ocean more closely, reflecting local atmospheric events such as local rainfall, while the MIMOC climatology and MOAA GPV products are bulk measurements representative of the ocean's upper 10 m. Under certain conditions, bulk and skin SSS values can be significantly different (Henocq et al., 2010).

SPATIAL PATTERNS

The MIMOC climatology (Figure 1a) clearly reveals differences in SSS-max patterns: the North and South Atlantic subtropical surface waters are the saltiest (in excess of 37), while the North Pacific SSS-max is the least salty (less than 36), and the South Pacific and southern Indian Oceans fall between the two extremes. The SSS-max of the North Atlantic and North Pacific are found within the 25° – 30° N latitude range; the South Atlantic and South Pacific SSS-maxima are closer to the equator, falling between 15° S and 20° S; and the southern Indian Ocean SSS-max near 30° S is the most poleward of the five regimes.

There are differences in where the SSS-max feature is situated within the anticyclonic subtropical gyres, as revealed by mean sea surface dynamic topography (Figure 1a; Maximenko et al., 2009). In all areas but the South Atlantic, the SSS-max falls fully within the equatorial-flowing limb of the subtropical gyre at the central or eastern sector of the subtropical belt. In the North and South Pacific, the SSS-max falls close to the apex of the sea surface dynamic topography ridge, marking the switchover from currents with an eastward component to those with a westward component, whereas in the North Atlantic, the geostrophic surface flow is strongly meridional. In the South Atlantic, there is a broad flow toward the northwest, with its SSS-max “pressed up” against the western boundary. In the western South Pacific, there is a secondary (weaker) SSS-max in the Tasman Sea near 30° S, at the same latitude band as the SSS-max of the southern Indian Ocean.

In all five regions, the strongest Ekman

transport (Figure 1a) within the open ocean is found within the trade wind belt, or equatorward of the SSS-max. The decreasing magnitude of the Ekman transport across the SSS-max imposes surface convergence, forcing downwelling of 20–40 m yr⁻¹ in the SSS-max region, defining the downward-flowing limb of the shallow subtropical meridional circulation cell with equatorward spreading of a subsurface salinity maximum core layer (O'Connor et al., 2005). The Ekman transport opposes and is of greater strength than the equatorward flowing surface geostrophic flow. In the eastern reach of the SSS-max, the Ekman transport vectors have a significant westward component, associated with eastern boundary upwelling, an attribute that is less evident in the North Pacific. The North and South Pacific have the freshest eastern boundary currents (California Current and Chile-Peru Current, respectively), both drawing water from their subpolar belts. The North Atlantic and southern Indian Oceans have the saltiest

eastern boundary currents, the Canary and Leeuwin Currents, respectively; in both cases, the low salinity subpolar water input is stymied by larger-scale circulation patterns, as discussed below.

Aquarius satellite SSS for the 24-month period of 2012–2013 (Figure 1b) displays a similar pattern as the MIMOC climatology, though the Aquarius SSS-max for the South Pacific is fresher, while the North Pacific SSS-max is saltier than the climatology (Figure 1a). Evaporation minus precipitation (E–P; Figure 1b) reveals the extent of net evaporation within the subtropics. In all regions, the maximum E–P occurs equatorward of the SSS-max, within the trade wind belt. Presumably, the salty products of net evaporation are shifted poleward by the large poleward Ekman transport, overwhelming the opposing surface geostrophic currents. In the western tropical Pacific, areas of negative E–P (dashed contours on Figure 1b) are found near 5°N and 10°S, separating a band of relatively salty surface water projecting westward along the

equator. The saltiest and larger SSS-max area is observed in the central and eastern South Pacific. The secondary SSS-max found in the western South Pacific near 30°S is more aligned with the southern Indian Ocean SSS-max than with the central South Pacific max. A trough of lower SSS separates these two regions near 170°W to 180°.

The mean SSS in all ocean basins varies strongly (Figure 1a). In order to compare the SSS patterns of each subtropical region, we subtract a constant salinity value (S-ref) within each domain (Figure 2a). In this study, the five reference values are derived from the MIMOC climatology and are kept constant for all other data sets shown, assuming that the climatology is the best representation of the mean state of the ocean. For each region, we derive a monthly SSS-max time series¹, with the lowest value of each series defining S-ref (Figure 2a; mean position in thick contour). Values of SSS greater than or equal to the S-ref were averaged and anomalies were referenced to S-ref; hence,

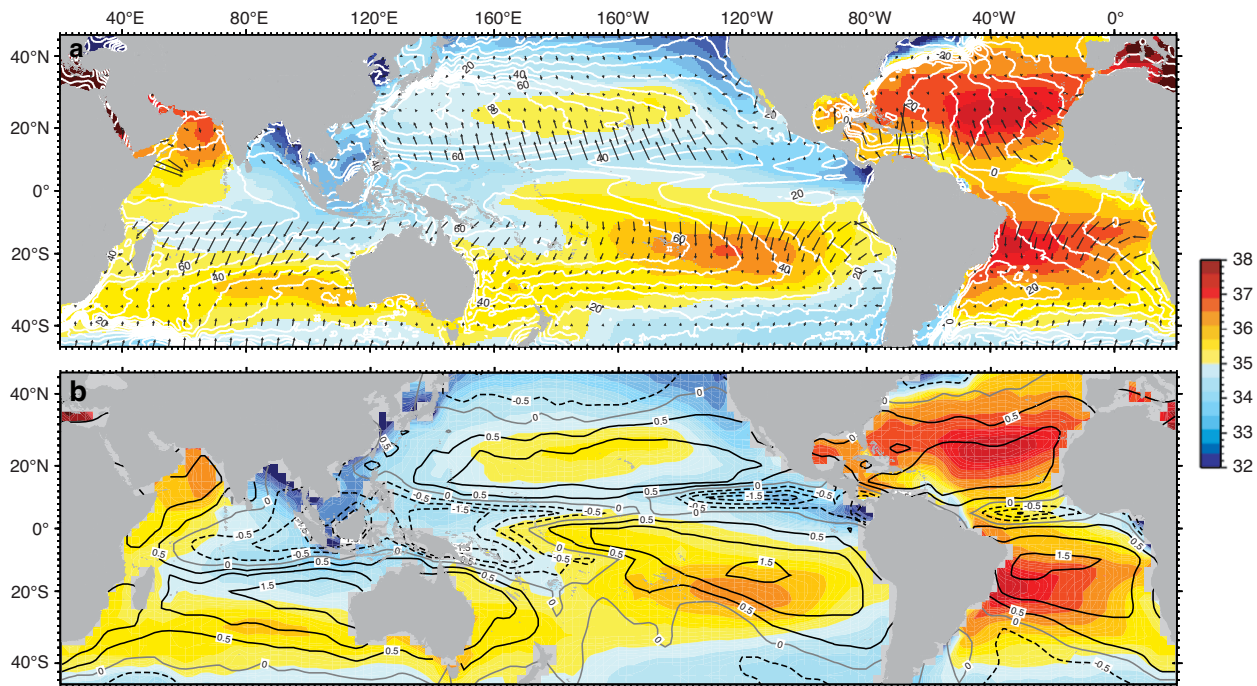


FIGURE 1. (a) Annual average sea surface salinity (SSS) climatology from the Monthly Isopycnal Mixed Layer Ocean Climatology (MIMOC; Schmidt et al., 2013) data in color. The white contours show the mean dynamic topography (MDOT; Maximenko et al., 2009) with a contour interval of 10 cm. The arrows represent the Ekman transport in Sverdrups ($Sv = 10^6 \text{ m}^3 \text{ s}^{-1}$), computed using ERA-40 wind stress data (Uppala et al. 2005). (b) Years 2012–2013 mean SSS from Aquarius v3.0 Level 3 bias adjusted data (available via the NASA PO.DAAC portal) in color and evaporation minus precipitation (E–P) in m yr^{-1} as contours, only plotting the -1.5 to 1.5 range, every 0.5 m yr^{-1} , $E > P$ with solid lines. Evaporation data from the WHOI OaFlux Project (<http://oafux.whoi.edu>) and precipitation from the GPCP v2.2 combined observations and satellite data (NASA's GPCP project at <http://precip.gsfc.nasa.gov>)

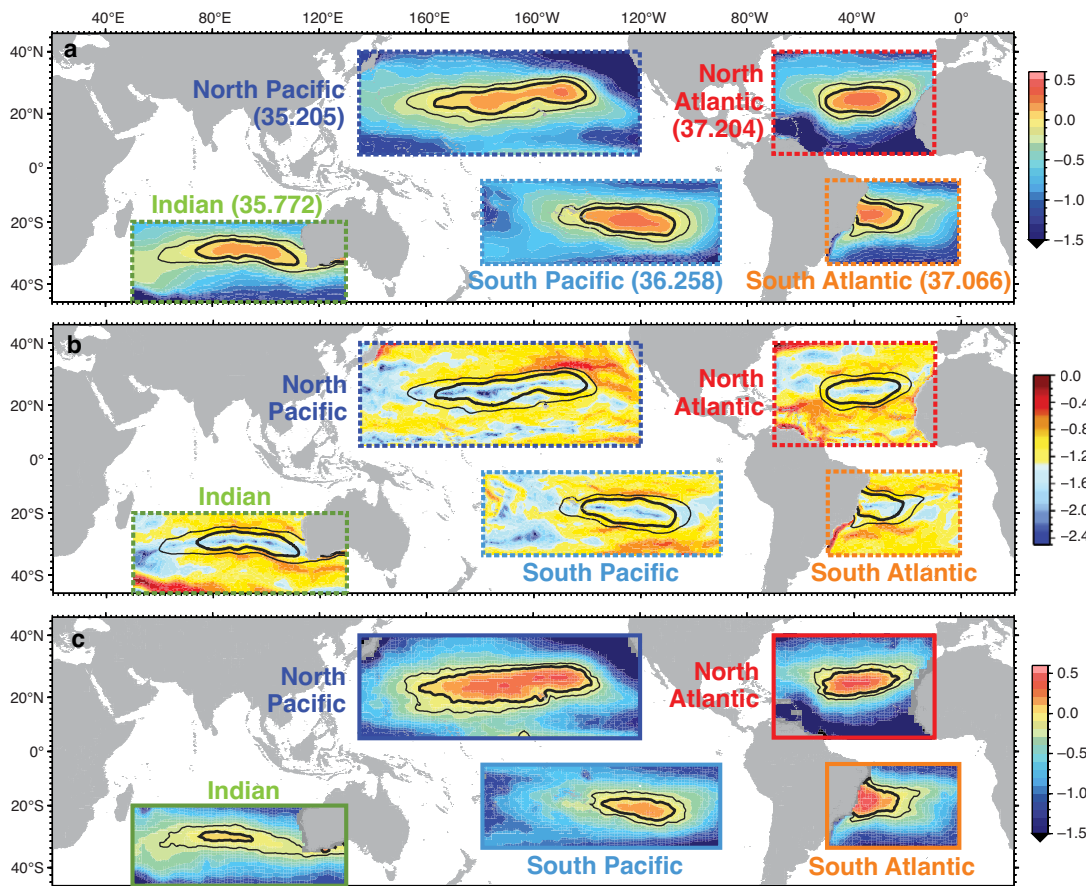


FIGURE 2. Subtropical surface salinity maximum (SSS-max) patterns. (a) Color patterns show the MIMOC climatological SSS anomalies within the five SSS-max subtropical regions. The anomalies are relative to a reference SSS indicated in parenthesis for each of the subtropical regions. The thin and thick contours denote the reference salinity (S-ref) and the -0.2 deviation from it. (b) Magnitude of the MIMOC SSS horizontal gradients (\log_{10}). The contours as shown in (a) are included. (c) Aquarius v3.0 Level 3 bias adjusted SSS anomalies for 2012–2013 in color. The contours are the same as in (a) but shown for the Aquarius data.

the values shown in Figures 3 and 4 are by definition positive, indicating the salinity contrast within the S-ref isohaline.

The SSS-max coincides with the minimum SSS gradient band (dark blue pattern in Figure 2b). As mentioned above, the climatological low SSS gradient regions in the North Atlantic and in the North Pacific are situated between 20°N and 30°N , centered near 26°N , whereas in the South Atlantic and South Pacific, the SSS-max regions are closer to the equator, between 15°S and 22°S , centered at 18°S , reflecting the general shift of the Intertropical Convergence Zone (ITCZ) to north of the equator within these ocean basins. The North and South Pacific SSS maxima tend to slope toward the equator from east to west. The North and South Atlantic SSS maxima display a similar trend, but to a lesser degree. The southern Indian SSS-max is the most poleward, falling near 26°S and 32°S , and

curves equatorward between 80°E and 90°E , but is flat west of that.

The North and South Atlantic SSS-max climatologies (Figure 2a) cover the smallest areas, yet display approximately the same range of SSS anomalies as the North and South Pacific, and they reveal greater contrast (“peakiness”) within the maxima regions (Figure 2b). The Indian sector displays the least variations from S-ref compared to all other sectors, with weak gradients that are almost comparable to those in the Pacific.

The Aquarius 2012–2013 subtropical SSS anomalies (Figure 2c) differ somewhat from the climatology (Figure 2a), not only showing variability of the maxima attained during that period but also in the extent of these regions. The Atlantic and North Pacific SSS anomalies within the reference isohaline contour (thicker black line) attain higher values, near 0.4 (Figure 2c), than the ~ 0.3 values

estimated from the climatology. The area of maximum salinity in the North Pacific also appears to be more widespread in the Aquarius data, while it is more limited in the MIMOC data set, particularly in the northeast of the region (Figure 2a,c). The South Pacific and southern Indian Ocean Aquarius anomalies are lower than the climatology (Figure 2a,c). While these differences of about 0.1 may reflect 2012–2013 conditions relative to climatology, they are within Aquarius uncertainty (Lagerloef, et al., 2013).

The SSS-max centroid positions (not shown), defined as the “center of mass” of all grid cells that are above the S-ref, were determined monthly for the MIMOC climatology and for the 2012–2013 Aquarius data. The monthly climatology centroids for all of the SSS-max regimes cluster within a more confined region than those estimated from Aquarius data, which display seasonal scatter that spans a

¹ The SSS-max is defined as the 94th percentile of SSS within each domain at each time step. We chose this method to enable comparison among data sets used in this study. When the absolute maximum of SSS is chosen instead, the area enclosed by the S-ref isohaline becomes very small or disappears intermittently in the other data sets due to interannual variability and lower spatial resolution.

wider range of longitudes. This is particularly the situation for the southern Indian Ocean, where the Aquarius monthly centroids fall within the longitude of 79°E to 94°E, whereas for the climatology, seasonal scatter is confined between 93° and 94°E. In the South Atlantic and South Pacific, the Aquarius centroids fall about 2° of latitude poleward of the climatological centroid. We suggest that these differences are due to the near synoptic coverage of the Aquarius data set relative to the MIMOC gridded product.

SEASONAL CYCLE AND INTERANNUAL FLUCTUATIONS

All of the SSS-max regions display a climatological seasonal cycle (Figure 3). Area averages within the salty confines of the constant S-ref isohaline are shown as differences relative to the constant reference salinity. While the value of the SSS anomaly varies with SSS-max, the North Pacific and southern Indian Oceans having the smallest SSS anomalies, the timing (after adjusting for the boreal and austral seasons) of the maximum and minimum SSS anomaly is similar for each SSS-max regime: a fall season maximum as summer conditions lead to increasing SSS and a spring season minimum

as winter relaxation of E–P allows ocean processes to rebuild the freshwater content (Gordon and Giulivi, 2014). All three of the southern SSS maxima tend to have broader SSS anomaly maxima and minima. The South Pacific displays a particularly large and broad SSS-anomaly spanning the months from April to August. A less regular seasonal cycle in the South Pacific (compare Figure 4) could manifest as a broader peak when the climatological average is computed, while the magnitude of the seasonal cycle might be slightly biased by the land mask that removes SSS values around the southwestern Pacific islands, leading to a S-ref that might be biased high.

The amplitude of the seasonal range of salinity for all five regimes within the areas bounded by the reference salinities is about 0.05, with the North Pacific having a slightly larger amplitude and the southern Indian Ocean displaying the smallest. In the North Atlantic, the seasonal anomalies vary from approximately 0.11 in April (boreal spring) to 0.16 in September (boreal late summer), with an average annual value of 0.13. The North Pacific values are near 0.06 in April and 0.12 in September, with an average annual value of 0.09. The lower seasonal

anomaly values mean that the North Pacific SSS-max has a lower salinity contrast than that of the North Atlantic.

The Southern Hemisphere seasonal cycles are less similar to each other than are their Northern Hemisphere counterparts. In the South Atlantic, seasonal anomalies vary from approximately 0.095 in October to 0.15 in May (austral spring) to 0.15 in May (austral fall), with an annual average of 0.12. Of all of the subtropical SSS-max regimes, the South Pacific displays the largest SSS anomalies, 0.17 from April to July (austral fall into winter) and 0.12 in November (austral spring) for an annual average of 0.15. The southern Indian Ocean displays the smallest anomalies, maximum of 0.1 in March (austral fall) and near 0.06 in September (austral late winter).

There have been many studies of the interannual and longer fluctuation of subtropical SSS (e.g., Leadbetter et al., 2007; Roemmich et al., 2007; Lukas et al., 2008; Durack et al., 2012). A detailed time series of SSS (Figure 4) is accumulating from Aquarius and Argo profiler fleet data. Aquarius salinity anomalies show a seasonal cycle of greater amplitude than those drawn from the Argo data (Figure 4). This may reflect the more complete spatial coverage offered by Aquarius, but it may be a consequence of the Aquarius data representing the sea surface while Argo surface values are measurements from depths greater than a meter.

For the two Northern Hemisphere SSS-max regimes, the seasonal cycles are similar, though 2013 is saltier than 2012 in the Aquarius data. As noted above, the Aquarius mean 2012–2013 SSS is saltier than the Northern Hemisphere SSS-max climatology (Figure 2). The Argo data indicate that the North Atlantic and North Pacific were both relatively salty in 2010.

In the Southern Hemisphere, Aquarius SSS portrays a slightly saltier South Atlantic in 2013, as also observed in the North Atlantic. The southern Indian Ocean displays the lowest salinity

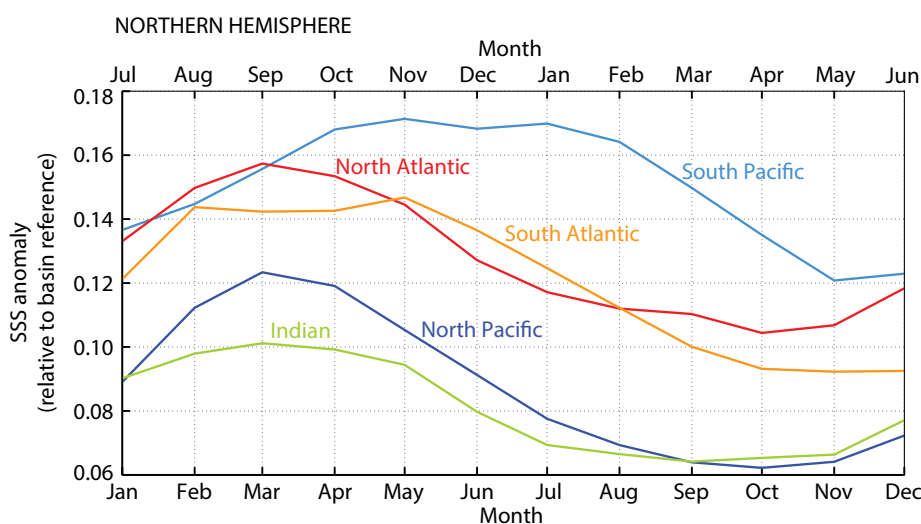


FIGURE 3. Seasonal cycle SSS anomaly for each ocean basin from MIMOC climatology data. Values represent the average for those latitude/longitude cells that have SSS equal to or higher than the basin reference (thick black contours in Figure 2a). Anomalies are referenced to each basin, permitting better comparison of seasonal cycles among the five subtropical regimes. Months of the year are shifted for six months between hemispheres to compensate for north/south seasonal phase shift.

anomaly, consistent with climatology, as mentioned above. However, the Aquarius SSS for the South Pacific exhibits a low salinity anomaly and weak seasonality (Figure 4), in contrast with the climatology (Figure 3), which shows the South Pacific as having the highest salinity anomaly. The Aquarius and JAMSTEC Argo South Pacific seasonalities are very different in phase, with peaks about three months apart. In the two Northern Hemisphere SSS-max regimes, the seasonal cycles are similar in phase. In the North Atlantic, it is relatively steady with only small variations in the peaks and troughs. The North Pacific exhibits more variation, with the Argo data showing a peak in boreal fall 2010.

DISCUSSION

While there are similarities in the five SSS-max regimes, they also display marked differences in their characteristics. Each has a slightly different “personality,” a likely consequence of the different land/ocean geometries of their ocean basins that affect SSS, such as E–P, mean circulation, and vertical and horizontal mixing processes (Vinogradova and Ponte, 2013; Busecke et al., 2014; Gordon and Giulivi, 2014). Additionally, each basin is linked in its own unique manner to global-scale, interocean circulation and overturning patterns (Gordon,

2001; Sprintall et al., 2013; Talley, 2013). In-depth, detailed study to explain the underlying causes of dissimilarities of the SSS-max regimes is needed. Here, we briefly point out aspects of the oceanographic settings of each of the five subtropical regions that are likely related to these dissimilarities. A more detailed view of SSS-max spatial and temporal characteristics will unfold as the Aquarius and SMOS (Font et al., 2010) satellite time series lengthen.

North Atlantic unique feature: the Atlantic Ocean is the saltiest of the five subtropical regions. Dry air blowing off the Sahara Desert leads to large freshwater fluxes out of the surface (Schanze et al., 2010) and thus high SSS values. The trade winds export the resultant water vapor across Central America into the tropical Pacific (Zaucker and Broecker, 1992). An additional factor, though not unrelated to the net water vapor export, is the Atlantic Meridional Overturning Circulation (AMOC). Relatively salty water from the South Atlantic is injected into the North Atlantic as a component of the upper limb of the AMOC. The North Atlantic subtropical eastern boundary current, the Canary Current, is notably saltier than those of the other basins (though the southern Indian Ocean has its own unique eastern boundary current,

the Leeuwin Current, discussed below) because the eastern limb of the North Atlantic subtropical gyre does not advect low-salinity subpolar water toward the equator as occurs in the North-South Pacific and South Atlantic. Rather, the subpolar region feeds into the lower limb of the AMOC.

South Atlantic unique feature: the South Atlantic SSS-max is located at the western sector of the subtropical belt. This feature is likely a consequence of the AMOC. Most of the South Equatorial Current (SEC) feeds into the cross-equatorial transport via the North Brazil Current, rather than turning southward into the South Atlantic subtropical western boundary Brazil current, becoming more concentrated in the regional salty subtropical water. The Benguela Current, the eastern boundary current of the South Atlantic subtropics, is fed by Indian Ocean subtropical water, with some inclusion of South Atlantic Current water (Gordon et al., 1992). A mixture of lower salinity Indian Ocean water, the Agulhas leakage, and subpolar water as parts of the South Atlantic Current curl into the Benguela Current (Beal et al., 2011). The SEC advects this water within a broad sweep toward the northwest, feeding into the cross-equatorial flow of the AMOC, “washing away” the SSS-max within the central and eastern subtropical sectors of the South Atlantic.

North Pacific unique feature: it is the freshest of the five SSS-max. The North Pacific has negative E–P due to input of water vapor from the Atlantic across Central America, and Southern Hemisphere water vapor into the ITCZ, near 10°N. Low SSS subpolar water is mainly injected into subtropical latitudes in the eastern boundary California Current, as export into the Arctic via Bering Strait is small <1 Sv (Roach et al., 1995), with the primary export of low salinity North Pacific water into the Indian Ocean within the Indonesian Throughflow (Gordon, 1986).

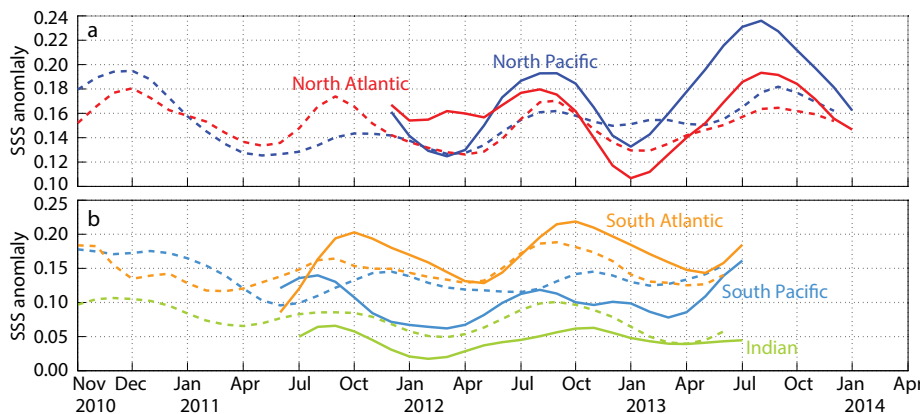


FIGURE 4. Interannual SSS anomaly time series for interannual data sets. The values are computed similarly to those in Figure 3. Values are smoothed using a four-month Gaussian window. The solid lines are Aquarius v3.0 Level 3 bias adjusted data and the dashed lines are from JAMSTEC Argo interpolated fields. (a) Northern Hemisphere. (b) Southern Hemisphere, with the time axis shifted six months to line up the seasonal cycles in both hemispheres.

South Pacific unique feature: it has a primary and secondary SSS-max. Within the central and eastern Pacific, the ITCZ is located north of the equator. However, in the western Pacific, there are two bands of high precipitation characteristic of the ITCZ, one north, the other south of the equator (Figure 1b; also see Figure 4 of Schanze et al., 2010). The southern ITCZ is more prominent during boreal winter and during La Niña years and is likely coupled to the increased presence of the western Pacific warm pool during these periods (Wallace and Hobbs, 2006, see their Figures 1.25, 10.21, and 10.25).

The South Pacific displays a large SSS anomaly and a broad seasonal cycle compared to the other four SSS-max regions (Figure 3). This may be due to the presence of a western South Pacific secondary SSS-max characteristic in the southwest corner of the primary South Pacific SSS-max box (Figure 2), or it may be related to the land-masking procedure that removes the SSS around the South Pacific islands, as mentioned above. Bingham et al. (2010), using ship-based, TAO/TRITON mooring, and Argo data, inspect the seasonality of the North and South Pacific SSS from 60°N to 40°S. They find that within the western tropical South Pacific near 15°S, the maximum SSS occurs in August/September, whereas more variable timing of the SSS-max occurs in the eastern South Pacific. This is likely a result of the details of the seasonal variability of the precipitation. The South Pacific is the only ocean basin with this kind of variable phase in the relevant latitude band (Bingham et al., 2012). However, as their in situ data coverage is sparse within the subtropical SSS-max of the South Pacific, inspection of the growing Aquarius and SMOS time series is needed to decipher the seasonality of the South Pacific SSS-max.

Southern Indian Ocean unique feature: the SSS-max exhibits a broad zonal band and is furthest from the equator. Similar to the western South Pacific, the Australia-Asian monsoon shifts the rainy

ITCZ into the Southern Hemisphere during the boreal winter (see Wallace and Hobbs, 2006, Figure 1.25). In addition, low salinity waters of the high precipitation Indonesian seas are injected into the eastern Indian Ocean near 12°S with the Indonesian Throughflow (Gordon, 1986); there is also low SSS advected into the region by the South Java Current, drawing water from the Bay of Bengal (Figure 1). The low SSS water spreads westward within the zonal-flowing South Equatorial Current, forcing the subtropical SSS-max water to reside well to the south of the high E-P band that lies slightly north of 20°S. The eastern boundary is relatively salty as low SSS subpolar water is not funneled northward by Australia, blocked by the southward-flowing Leeuwin Current. Additionally, Tasman leakage allows salty subtropical water from the Great Australian Bight to spread into the Indian Ocean (van Sebille et al., 2014). The western boundary Agulhas Current injects salty water from the evaporative western Indian Ocean into the southern subtropical belt.

CONCLUSIONS

The subtropical ocean SSS maxima of the North and South Atlantic, the North and South Pacific, and the southern Indian Oceans constitute integrated responses to excess evaporative air-sea freshwater flux and convergence of freshwater by ocean circulation and mixing processes, and they display similarities and differences. The five subtropical regimes all have slightly different “personalities” that likely are consequences of specific land/ocean regional geometries. The basins are not isolated from the larger ocean; each is linked in its own unique manner to global-scale interocean circulation and overturning patterns. We introduce a simple methodology that enables comparison of SSS-max features with each other globally, reducing the impact of arbitrarily chosen isohalines to define SSS maxima.

Our descriptive discussion of the SSS-max regimes and underlying causes

of dissimilarities is meant to inform the general readership of the uniqueness of each SSS-max regime and to encourage in-depth, comparative study in order to fully understand the governing forces that shape the SSS-max subtleties and their places within the global hydrological system. Insights into the nature of the spatial and temporal characteristics of SSS patterns will no doubt be further enabled as the Aquarius and the SMOS time series grow. 

ACKNOWLEDGEMENTS. NASA Grant Number NNX14AI90G to Lamont-Doherty; NASA under grant numbers NNX09AU70G and NNX11AE83G to UNCW. Lamont-Doherty Contribution Number 7846.

REFERENCES

- Beal, L.M., W.P.M. De Ruijter, A. Biastoch, R. Zahn, M. Cronin, J. Hermes, J. Lutjeharms, G. Quartly, T. Tozuka, S. Baker-Yeboah, and others. 2011. On the role of the Agulhas system in ocean circulation and climate. *Nature* 472:429–436, <http://dx.doi.org/10.1038/nature09983>.
- Bingham, F.M., G.R. Foltz, and M.J. McPhaden. 2010. Seasonal cycles of surface layer salinity in the Pacific Ocean. *Ocean Science* 6:775–787, <http://dx.doi.org/10.5194/os-6-775-2010>.
- Bingham, F.M., G.R. Foltz, and M.J. McPhaden. 2012. Characteristics of the seasonal cycle of surface layer salinity in the global ocean. *Ocean Science* 8:915–929, <http://dx.doi.org/10.5194/os-8-915-2012>.
- Busecke, J., A.L. Gordon, Z. Li, F.M. Bingham, and J. Font. 2014. Subtropical surface layer salinity budget and the role of mesoscale turbulence. *Journal of Geophysical Research* 119:4,124–4,140, <http://dx.doi.org/10.1002/2013JC009715>.
- Durack, P.J., S.E. Wijffels, and R.J. Matear. 2012. Ocean salinities reveal strong global water cycle intensification during 1950 to 2000. *Science* 336:455–458, <http://dx.doi.org/10.1126/science.1212222>.
- Font, J., A. Camps, A. Borges, M. Martin-Neira, J. Boutin, N. Reul, Y.H. Kerr, A. Hahne, and S. Mecklenburg. 2010. SMOS: The challenging sea surface salinity measurement from space. *Proceedings of the IEEE* 98:649–665, <http://dx.doi.org/10.1109/JPROC.2009.2033096>.
- Gordon, A.L. 1986. Inter-ocean exchange of thermocline water. *Journal of Geophysical Research* 91(C4):5,037–5,046, <http://dx.doi.org/10.1029/JC091iC04p05037>.
- Gordon, A.L., R.F. Weiss, W.M. Smethie Jr., and M.J. Warner. 1992. Thermocline and intermediate water communication between the South Atlantic and Indian Oceans. *Journal of Geophysical Research* 97(C5):7,223–7,240, <http://dx.doi.org/10.1029/92JC00485>.
- Gordon, A.L. 2001. Inter-ocean exchange. Pp. 305–314 in *Ocean Circulation and Climate*. G. Siedler, S. Griffies, J. Gould, and J. Church, eds, Academic Press.
- Gordon, A.L., and C.F. Giulivi. 2014. Ocean eddy freshwater flux convergence into the North Atlantic Subtropics. *Journal of Geophysical Research* 119:3,327–3,335, <http://dx.doi.org/10.1002/2013JC009596>.

- Henocq, C., J. Boutin, G. Reverdin, F. Petitcolin, S. Arnault, and P. Lattes. 2010. Vertical variability of near-surface salinity in the tropics: Consequences for I-band radiometer calibration and validation. *Journal of Atmospheric and Oceanic Technology* 27:192–209, <http://dx.doi.org/10.1175/2009JTECHO670.1>.
- Hosoda, S., T. Ohira, T. Nakamura. 2008. A monthly mean dataset of global oceanic temperature and salinity derived from Argo float observations. *JAMSTEC Report of Research and Development* 8:47–59.
- Koltermann, K.P., V.V. Gouretski, and K. Jancke. 2011. *Hydrographic Atlas of the World Ocean Circulation Experiment (WOCE): Volume 3. Atlantic Ocean*. M. Sparrow, P. Chapman, and J. Gould, eds, International WOCE Project Office, Southampton, UK.
- Lagerloef, G., F.R. Colomb, D. Le Vine, F. Wentz, S. Yueh, C. Ruf, J. Lilly, J. Gunn, Y. Chao, A. deCharon, and others. 2008. The Aquarius/SAC-D Mission: Designed to meet the salinity remote-sensing challenge. *Oceanography* 21:68–81, <http://dx.doi.org/10.5670/oceanog.2008.68>.
- Lagerloef, G. 2012. Satellite mission monitors ocean surface salinity. *Eos, Transactions American Geophysical Union* 93(25):233, <http://dx.doi.org/10.1029/2012EO250001>.
- Lagerloef, G., F. Wentz, S. Yueh, H.Y. Kao, G.C. Johnson, and J.M. Lyman. 2012. Aquarius satellite mission provides new, detailed view of sea surface salinity. Pp. S70–71 in *State of the Climate in 2011*. J. Blunden and D.S. Arndt, eds, Special Supplement to the Bulletin of the American Meteorological Society, vol. 93(7).
- Lagerloef, G., S. Yueh, and J. Piepmeier. 2013. Review & forecast: NASA's Aquarius Mission provides new ocean view. *Sea Technology* 54(1), <http://www.sea-technology.com/features/2013/0113/NASA.php>.
- Leadbetter, S.J., R.G. Williams, E.L. McDonagh, and B.A. King. 2007. A twenty year reversal in water mass trends in the subtropical North Atlantic. *Geophysical Research Letters* 34, L12608, <http://dx.doi.org/10.1029/2007GL029957>.
- Lukas, R., and F. Santiago-Mandujano. 2008. Interannual to interdecadal salinity variations observed near Hawaii: Local and remote forcing by surface freshwater fluxes. *Oceanography* 21(1):46–55, <http://dx.doi.org/10.5670/oceanog.2008.66>.
- Maximenko, N., P. Niiler, M.-H. Rio, O. Melnichenko, L. Centurioni, D. Chambers, V. Zlotnicki, and B. Galperin. 2009. Mean dynamic topography of the ocean derived from satellite and drifting buoy data using three different techniques. *Journal of Atmospheric and Oceanic Technology* 26:1,910–1,919, <http://dx.doi.org/10.1175/2009JTECHO672.1>.
- McCreary, J., and P. Lu. 1994. On the interaction between the subtropical and equatorial ocean circulations: The subtropical cell. *Journal of Physical Oceanography* 24:466–497.
- Meissner, T., F. Wentz, L. Ricciardulli, and K. Hilburn. 2014. The Aquarius salinity retrieval algorithm recent progress and remaining challenges. Pp. 49–54 in *13th Specialist Meeting on Microwave Radiometry and Remote Sensing of the Environment (MicroRad)*. March 24–27, 2014, <http://dx.doi.org/10.1109/MicroRad.2014.6878906>.
- O'Connor, B.M., R. Fine, and D.B. Olson. 2005. A global comparison of subtropical underwater formation rates. *Deep Sea Research Part I* 52:1,569–1,590, <http://dx.doi.org/10.1016/j.dsr.2005.01.011>.
- Roach, A.T., K. Aagaard, C.H. Pease, S.A. Salo, T. Weingartner, V. Pavlov, and M. Kulakov. 1995. Direct measurements of transport and water properties through Bering Strait. *Journal of Geophysical Research* 100:18,443–18,457, <http://dx.doi.org/10.1029/95JC01673>.
- Roemmich, D., J. Gilson, R. Davis, P. Sutton, S. Wijffels, and S. Riser. 2007. Decadal spinup of the South Pacific subtropical gyre. *Journal of Physical Oceanography* 37:162–173, <http://dx.doi.org/10.1175/JPO3004.1>.
- Schanze, J.J., R.W. Schmitt, and L.L. Yu. 2010. The global oceanic freshwater cycle: A state of the art quantification. *Journal of Marine Research* 68:569–575, <http://dx.doi.org/10.1357/002224010794657164>.
- Schmidtke, S., G.C. Johnson, and J.M. Lyman. 2013. MIMOC: A global monthly isopycnal upper-ocean climatology with mixed layers. *Journal of Geophysical Research* 118:1,658–1,672, <http://dx.doi.org/10.1002/jgrc.20122>.
- Schmitt, R.W. 1995. The ocean component of the global water cycle. *Reviews of Geophysics* 33(S2):1,395–1,409, <http://dx.doi.org/10.1029/95RG00184>.
- Schmitt, R.W. 2008. Salinity and the global water cycle. *Oceanography* 21(1):12–19, <http://dx.doi.org/10.5670/oceanog.2008.63>.
- Sprintall, J., G. Siedler, and H. Mercier. 2013. Inter-ocean and interbasin exchanges. Chapter 19 in *Ocean Circulation and Climate: A 21st Century Perspective*. G. Siedler, S. Griffies, J. Gould, and J. Church, eds, Elsevier Science & Technology, <http://dx.doi.org/10.1016/B978-0-12-391851-2.00019-2>.
- Talley, L.D. 2002. Salinity patterns in the ocean. Pp. 629–640 in *Encyclopedia of Global Environmental Change (vol. 1): The Earth System*. Physical and Chemical Dimensions of Global Environmental Change. M.C. MacCracken and J.S. Perry, eds, John Wiley and Sons.
- Talley, L.D. 2007. *Hydrographic Atlas of the World Ocean Circulation Experiment (WOCE): Volume 2. Pacific Ocean*. M. Sparrow, P. Chapman, and J. Gould, eds, International WOCE Project Office, Southampton, UK.
- Talley, L.D. 2008. Freshwater transport estimates and the global overturning circulation: shallow, deep and throughflow components. *Progress in Oceanography*, 78:257–303, <http://dx.doi.org/10.1016/j.pocean.2008.05.001>.
- Talley, L.D. 2011. *Hydrographic Atlas of the World Ocean Circulation Experiment (WOCE): Volume 4. Indian Ocean*. M. Sparrow, P. Chapman, and J. Gould, eds, International WOCE Project Office, Southampton, UK, http://www-pord.ucsd.edu/whp_atlas/indian_index.html.
- Talley, L.D., G.L. Pickard, W.J. Emery, and J.H. Swift, eds. 2011. *Descriptive Physical Oceanography: An Introduction*, 6th ed. Elsevier, Boston, MA, USA, 560 pp.
- Talley, L.D. 2013. Closure of the global overturning circulation through the Indian, Pacific, and Southern Oceans: Schematics and transports. *Oceanography* 26(1):80–97, <http://dx.doi.org/10.5670/oceanog.2013.07>.
- Uppala, S.M., P.W. Kållberg, A.J. Simmons, U. Andrae, V. Da Costa Bechtold, M. Fiorino, J.K. Gibson, J. Haseler, A. Hernandez, G.A. Kelly, and others. 2005. The ERA-40 re-analysis. *Quarterly Journal of the Royal Meteorological Society* 131:2,961–3,012, <http://dx.doi.org/10.1256/qj.04.176>.
- Vinogradova, N.T., and R.M. Ponte. 2013. Clarifying the link between surface salinity and freshwater fluxes on monthly to interannual time scales. *Journal of Geophysical Research* 118:3,190–3,201, <http://dx.doi.org/10.1002/jgrc.20200>.
- van Sebille, E., J. Sprintall, F.U. Schwarzkopf, A.S. Gupta, A. Santoso, M.H. England, A. Biastoch, and C.W. Boning. 2014. Pacific-to-Indian Ocean connectivity: Tasman leakage, Indonesian Throughflow, and the role of ENSO. *Journal of Geophysical Research Oceans*, 119:1,365–1,382, <http://dx.doi.org/10.1002/2013JC009525>.
- Wallace, J., and P. Hobbs. 2006. *Atmospheric Science: An Introductory Survey*, 2nd ed. International Geophysics Series, vol. 92, 483 pp.
- Zaucker, F., and W. Broecker. 1992. The influence of atmospheric moisture transport on the fresh water balance of the Atlantic drainage basin. *Journal of Geophysical Research* 97:2,765–2,773, <http://dx.doi.org/10.1029/91JD01699>.

AUTHORS. Arnold L. Gordon (agordon@deo.columbia.edu) is Professor, Claudia F. Giulivi is Senior Staff Associate, and Julius Busecke is PhD Candidate, all at Lamont-Doherty Earth Observatory of Columbia University, Palisades, NY, USA. Frederick M. Bingham is Professor, Center for Marine Science, University of North Carolina Wilmington, Wilmington, NC, USA.

ARTICLE CITATION

Gordon, A.L., C.F. Giulivi, J. Busecke, and F.M. Bingham. 2015. Differences among subtropical surface salinity patterns. *Oceanography* 28(1):32–39, <http://dx.doi.org/10.5670/oceanog.2015.02>.